



Geophysical Research Letters*

RESEARCH LETTER

10.1029/2021GL096192

Key Points:

- Organization of Tropical East Pacific Convection field campaign observations indicate shallow (5°N) and deep (8°N) ascending motion over the East Pacific intertropical convergence zone (ITCZ)
- Reanalysis (satellite) products show predominant shallow (deep) ascending motion across the East Pacific ITCZ
- Reanalysis and satellite products by themselves are insufficient for characterizing convection over this region

Supporting Information:

Supporting Information may be found in the online version of this article.

Correspondence to:

L. Huaman, lidiana.huaman@tamu.edu

Citation:

Huaman, L., Schumacher, C., & Sobel, A. H. (2022). Assessing the vertical velocity of the East Pacific ITCZ. *Geophysical Research Letters*, 49, e2021GL096192. https://doi.org/10.1029/2021GL096192

Received 15 SEP 2021 Accepted 1 DEC 2021

Assessing the Vertical Velocity of the East Pacific ITCZ

Lidia Huaman¹, Courtney Schumacher¹, and Adam H. Sobel^{2,3}

¹Department of Atmospheric Sciences, Texas A&M University, College Station, TX, USA, ²Department of Applied Physics and Applied Mathematics, Columbia University, New York, NY, USA, ³Lamont-Doherty Earth Observatory, Columbia University, New York, NY, USA

Abstract Reanalysis and satellite data sets disagree on the vertical structure of the meridional overturning circulation over the East Pacific (EP) intertropical convergence zone (ITCZ). Recent observations from the Organization of Tropical East Pacific Convection (OTREC) 2019 field campaign show a meridional slope of vertical motion with a shallow mode from 3° to 7°N, over a strong meridional sea surface temperature (SST) gradient, and a deeper mode from 7° to 10.5°N, where the SST is predominantly warm. However, reanalysis fields from the OTREC period show a predominant shallow mode from 3° to 9°N unless OTREC dropsondes are assimilated; then a weak deep mode is found at 8°N. Vertical motion over the OTREC region derived from Global Precipitation Measurement (GPM) precipitation radar latent heating retrievals has the opposite problem in that the deep mode is predominant from 3° to 10°N. A shallow mode is present with the addition of cloud radar data.

Plain Language Summary There is no consensus on where air rises most strongly and to what heights over the tropical East Pacific Ocean because there are very few available in situ observations. Thus, we rely on numerical models or satellite observations to make estimates of where air rises and where storms are deepest and strongest. In this study, we show recent field campaign observations that indicate the existence of two modes of upward motion: a shallow mode (i.e., ascending motion up to 4 km AMSL) in the southern part of the main precipitation band just north of the equator, and a deep mode (i.e., ascending motion up to 10 km AMSL) a few hundred km farther north. While numerical models only produce the shallow mode, satellite algorithms suggest only a deep mode. Improvements were made when the numerical models used in situ data for guidance and the satellite algorithms were supplemented with observations from other sensors. In situ observations were crucial to conclude that currently available numerical model and satellite data sets, independently, are problematic for describing the large-scale air motions in the East Pacific.

1. Introduction

The vertical structure of the vertical velocity in the East Pacific (EP) intertropical convergence zone (ITCZ) has been highly debated, mainly because of the disagreement between reanalysis and satellite data sets (e.g., Hagos et al., 2010). While satellite-based studies show a predominance of deep ascending motion associated with deep convection (Liu et al., 2015; Schumacher et al., 2004), reanalyzes suggest strong shallow ascending motion (Back & Bretherton, 2006; Yokoyama et al., 2014). Schumacher et al. (2004) used observations from the precipitation radar aboard the Tropical Rainfall Measurement Mission (TRMM) satellite to estimate vertical profiles of latent heating and showed top-heavy heating associated with deep ascending motion in the EP ITCZ. Back and Bretherton (2006) used ERA-40 and NCEP-NCAR reanalyzes to study the vertical structure of the EP ITCZ and showed maximum ascending motion at 850 hPa associated with an import of moist static energy (MSE) through vertical advection. This shallow ascending motion is linked to a shallow meridional overturning circulation in the southern part of the EP ITCZ and is supported by the East Pacific Investigation of Climate Processes in the Coupled Ocean–Atmosphere System (EPIC-2001) field campaign data set (Zhang et al., 2004).

In a more recent study using EPIC-2001 and other in situ data, Huaman and Takahashi (2016) showed a second vertical motion peak above the shallow ascending motion peak. Additionally, Huaman and Schumacher (2018) used 16 years of CloudSat and TRMM satellite radar observations to estimate vertical profiles of latent heating in the EP ITCZ. They combined shallow precipitation from the CloudSat W-band radar and deep (i.e., convective and stratiform) precipitation from the TRMM K_u -band radar to more accurately represent latent heating from the full convective spectrum. Their results demonstrated that two peaks of latent heating associated with deep and shallow ascending motion are apparent in this region and linked to deep and shallow meridional circulations

© 2021. American Geophysical Union. All Rights Reserved.

HUAMAN ET AL. 1 of 10



(Nolan et al., 2007). They also found that the vertical structure of the EP ITCZ is tilted meridionally; shallow ascending motion occurs around 6°N in the southern part of the ITCZ and transitions to deep ascending motion around 9°N in the northern part of the ITCZ. Using reanalysis data, Trenberth et al. (2000) also identified the shallow and deep mode in the global monsoon, including in the EP ITCZ. The shallow and deep modes over the EP ITCZ experiences interannual, seasonal, and synoptic variability (Huaman et al., 2021; Zhang et al., 2008). Schumacher et al. (2004) showed an increase of stratiform rain fraction (and thus a deeper vertical mode) during El Niño years over this region. Huaman and Schumacher (2018) studied the seasonal variability of the vertical velocity associated with convection in the EP ITCZ and found a predominance of the shallow mode during boreal winter and spring, and deep and shallow mode during boreal summer and fall. Additionally, Huaman et al. (2020) showed that convectively coupled Kelvin waves impact the meridional circulation in the EP ITCZ, enhancing the shallow ascending motion ahead of the Kelvin wave and deep ascending motion within the Kelvin wave.

The vertical structure of the meridional circulation is important to the MSE budget, and thus to the theoretical questions about the relationship of convection to large-scale dynamics (Frierson, 2007; Inoue & Back, 2015; Neelin & Held, 1987; Numaguti, 1993; Raymond et al., 2009; Sobel, 2007; Yu et al., 1998). However, it has been a challenge to determine which data set among reanalyzes and satellite products is closer to the truth because of the lack of in situ observations over the EP. The lack of in situ observations causes reanalysis data sets to rely heavily on the physical parameterizations of models that might not represent the actual conditions. Additionally, latent heating algorithms from the TRMM and Global Precipitation Measurement (GPM) satellites are based on look-up tables from cloud-resolving models (CRMs) that might not be representative of the EP ITCZ. Therefore, more studies based on in situ observations are needed to improve our understanding of the vertical velocity and convection over this region and examine the reliability of vertical motion from multiple reanalyzes and satellite products. In this study, we analyze the vertical velocity observed during the Organization of Tropical East Pacific Convection (OTREC 2019; Fuchs-Stone et al., 2020) field campaign to determine which product among four common reanalyzes is closer to the OTREC observations and thus more likely to represent the true meridional overturning structure in the EP ITCZ.

2. Data and Methodology

We used observationally based vertical velocity (i.e., vertical pressure velocity in Pa s⁻¹) from an OTREC 3DVar analysis processed by New Mexico Tech (Fuchs-Stone et al., 2020), which was generated from gridded dropsonde data collected from NSF/NCAR Gulfstream V flights between 12 and 18 UTC (06 and 12 local time) to capture the morning peak of convection over ocean. Flight operations took place from 5 August to 3 October 2019 and 12 research flights (RFs) were performed over the EP OTREC flight box (89°–86°W, 3°–11°N; Figure 1a). However, we only considered nine research flights: RF02 (12 August), RF05 (17 August), RF08 (23 August), RF14 (21 September), RF16 (24 September), RF18 (27 September), RF19 (28 September), RF21 (1 October), and RF22 (2 October), which are shown as individual events in Figure S1 in Supporting Information S1. RF01 (7 August) and RF20 (30 September) were excluded because their extreme precipitation deviated significantly from the other RFs and from the precipitation climatology calculated using daily IMERG precipitation data (Huffman et al., 2015) from 1998 to 2019. RF11 (4 September) was also excluded due to missing data north of 8°N.

Vertical velocity fields were obtained from the following reanalyzes: ERA5, MERRA-2, JRA-55, and NCEP-NCAR. Reanalysis data was obtained for each RF day as well as for a large sample during August and September 2014–2020 (representing the climatological OTREC period). The sample criteria is explained in Section 4. Additionally, we only analyze reanalysis data during the OTREC flight times (12–18 UTC) in order to exclude variations in vertical motion due to the diurnal cycle (not shown). Table 1 lists the spatial and temporal resolution and convection and assimilation schemes for each reanalysis. We interpolated all the reanalyzes to 0.5° for comparison of specific latitudinal ranges, but note that JRA-55 and NCEP-NCAR have significantly coarser resolution than this.

We also obtained latent heating retrievals from the GPM radar. The GPM satellite was launched in 2014 (Hou et al., 2014) and is equipped with a dual-wavelength radar that provides the observational basis of the latent heating retrievals. The swath width of the radar is relatively narrow (245 km) and the satellite orbit (i.e., approximately 90 min) precesses through the diurnal cycle, which limits sampling over the OTREC flight box especially when only morning overpasses are considered to be consistent with the OTREC flight times. As such,

HUAMAN ET AL. 2 of 10



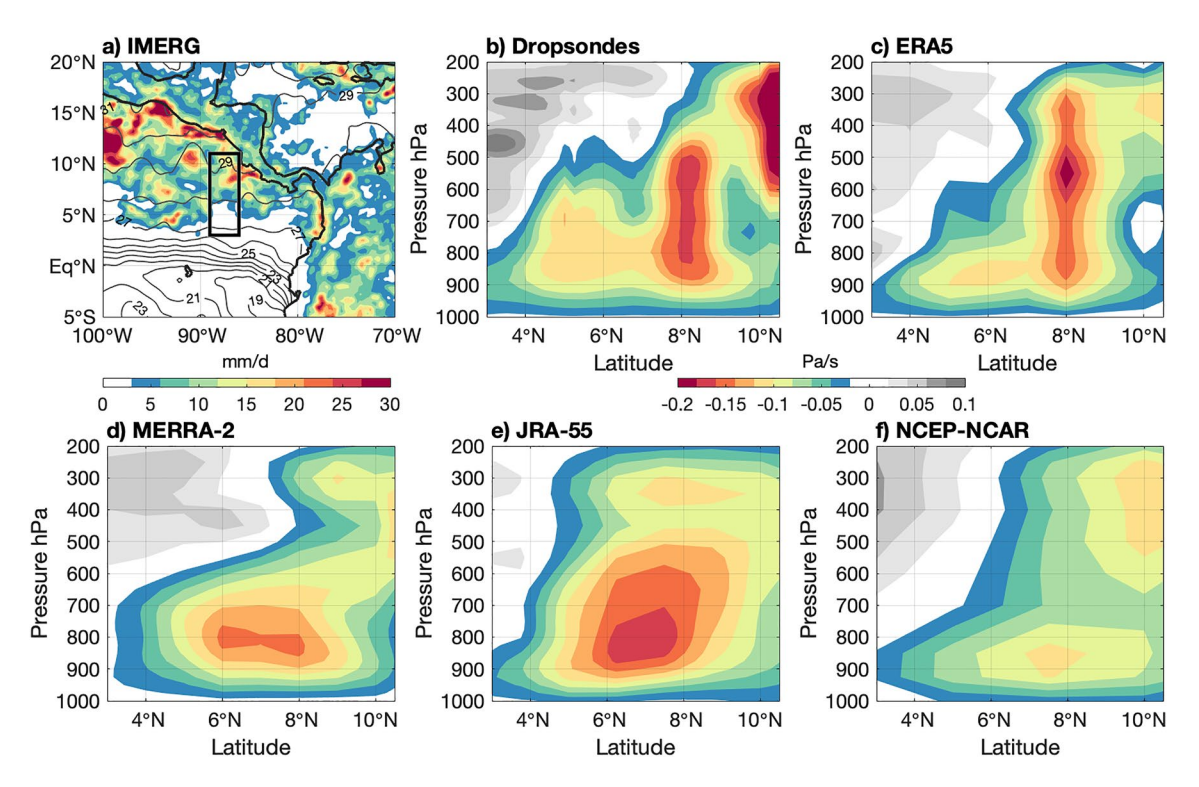


Figure 1. (a) Precipitation from IMERG in mm d^{-1} (shaded) and SST from OSTIA in C° (contours) averaged over the OTREC nine RF dates in 2019 and 12–18 UTC. The black box indicates the OTREC flight box. (b–f) Vertical cross sections of vertical motion in Pa s⁻¹ across 89°–86°W from OTREC dropsondes and the four analyzed reanalyzes (ERA5, MERRA-2, JRA-55, and NCEP-NCAR) averaged over the OTREC nine RF dates in 2019 and 12–18 UTC.

only one RF was sampled by the GPM radar during OTREC so we use all GPM orbital samples during August and September 2014–2020 between 12 and 18 UTC to calculate OTREC satellite profile statistics. The GPM latent heating algorithms used are: Convective Stratiform Heating (CSH), Spectral Latent Heating (SLH), and a novel algorithm developed by Huaman and Schumacher (2018; HS2018). The resolution and input data for the algorithms are detailed in Table 1. Hourly precipitation from IMERG and daily SST from the Operational Sea Surface Temperature and Ice Analysis (OSTIA, Donlon et al., 2012) were also used during the OTREC period.

Vertical velocity was estimated from the GPM latent heating retrievals using the thermodynamic equation: $\frac{d\ln(\theta)}{dt} + \overrightarrow{V}.\overrightarrow{\nabla}\theta + w\frac{d\ln(\theta)}{dz} = \frac{LH}{T}$, where $w = \frac{1}{\rho g}\left(\frac{dp}{dt} + \overrightarrow{V}.\overrightarrow{\nabla}p - \omega\right)$, p is pressure, \overrightarrow{V} is horizontal wind, g is the gravitational force, ρ is density, θ is potential temperature, z is height, LH is latent heating, and T is the air temperature. It is important to mention that vertical velocity is purely derived from latent heating and radiative cooling is disregarded in the simplified thermodynamic equation, which could lead to overestimation of vertical velocity from GPM algorithms at upper levels. Additionally, assuming that the vertical advection of potential temperature balances the latent heating (i.e., neglecting horizontal advection, turbulent diffusion, and radiative tendencies; Houze, 1989) and that the local pressure tendency and horizontal advection of pressure $\left(\frac{dp}{dt} + \overrightarrow{V}.\overrightarrow{\nabla}p \approx 0\right)$ are negligible (i.e., hydrostatic balance), the equation is simplified to $-\frac{\omega}{\rho g}\frac{d\ln(\theta)}{dz} = \frac{LH}{T}$. T and θ were obtained from ERA-5 and the results are not sensitive to the temperature used from different reanalyzes. It is important to mention that these assumptions may result in small deviations of GPM vertical velocity especially in the southern region of the ITCZ and high levels where the vertical ascending motion is weak.

3. Vertical Velocity During OTREC

Figure 1a shows the average IMERG precipitation across the EP for the nine analyzed OTREC RF dates. In the OTREC flight box, the maximum precipitation was located north of 7°N, where SST is warmest. During the OTREC period, the average precipitation was fairly consistent with the IMERG precipitation climatology from 1998 to 2014 (not shown) and there were no significant interannual (e.g., El Niño) events during OTREC. Some intraseasonal variability was observed, three weak-to-moderate Madden Julian Oscillation (MJO) events

HUAMAN ET AL. 3 of 10



Reanalysis	Resolution	Convective scheme	Assimilation scheme
ERA-5 Hersbach et al. (2020)	$0.28^{\circ} \times 0.28^{\circ}$, 1 hr	Upgraded mass flux	4D-Var
	137 pressure levels	Tiedtke (1989)	
MERRA-2 Gelaro et al. (2017)	$0.5^{\circ} \times 0.625^{\circ}$, 3 hr	Relaxed Arakawa-Schubert	3D-Var
	72 pressure levels	Moorthi and Suarez (1992)	
JRA-55 Kobayashi et al. (2015)	$1.25^{\circ} \times 1.25^{\circ}$, 6 hr	Prognostic Arakawa-Schubert	4D-Var
	37 pressure levels	Arakawa and Schubert (1974)	
NCEP-NCAR Saha et al. (2014)	$2.5^{\circ} \times 2.5^{\circ}$, 6 hr	Simplified Arakawa-Schubert	3D-Var
	17 pressure levels	Pan and Wu (1995)	
GPM Algorithm	Resolution	Satellite input	Heating look-up table
CSH V06 Tao et al. (2001), (2010)	$0.25^{\circ} \times 0.25^{\circ}$, 80 levels	Surface precipitation	CRM
		Rain type (shallow, convective, stratiform, anvil)	
		Echo-top height	
		Low-level reflectivity gradient	
SLH V06B Shige et al. (2004), (2007), (2009)	$0.25^{\circ} \times 0.25^{\circ}$, 80 levels	Surface precipitation	CRM
		Rain type (shallow, convective, stratiform, anvil)	
		Echo-top height	
		Melting level	
HS2018 Huaman and Schumacher (2018)	$0.25^{\circ} \times 0.25^{\circ}$, 80 levels	Melting level Surface precipitation	Obs

occurred based on the OLR MJO index (Kiladis et al., 2014). The mean vertical structure of the vertical velocity from OTREC dropsondes and reanalyzes during the nine RFs averaged for 12–18 UTC is shown in Figures 1b–1f. The spatial resolution of the reanalyzes ranges from 0.28° to 2.5°; therefore, the vertical velocities values are smoother in the reanalyzes with lower resolution.

The vertical velocity retrieved from OTREC observations (Figure 1b) suggests a meridional slope with shallow vertical motion between 4°N and 7°N, and deepening farther north at 8°N in the lower and mid troposphere and at 10.5°N in the mid and upper troposphere, consistent with Huaman and Takahashi (2016) and Huaman and Schumacher (2018). The meridional structure of vertical motion during OTREC was generally captured by ERA5 (Figure 1c), which shows weak shallow upward motion centered at 6°N and strong deep upward motion at 8°N. ERA5 assimilated OTREC dropsonde data, thus helping it capture the observed vertical motion structure, although the upward motion between 600 and 200 hPa at 10.5°N is much weaker in ERA5 compared to the OTREC dropsonde retrieval. JRA-55 (Figure 1e) also assimilated the OTREC dropsondes (Japan Meteorological Agency, personal communication), but its vertical motion is less consistent with OTREC observations. MERRA-2 and NCEP-NCAR (Figures 1d and 1f) did not assimilate OTREC in situ data (NASA/GSFC for MERRA-2 and National Centers for Environmental Prediction for NCEP-NCAR, personal communication) and exhibit predominantly shallow vertical motion around 7°N and weaker deep vertical motion around 10°N. The weak vertical motion in NCEP-NCAR is likely in part due to the 2.5° × 2.5° resolution, which smooths the vertical velocity values.

The different vertical motion structures between the reanalyzes can be attributed to the range of resolutions, convective schemes, and/or assimilation methods employed (Table 1); however, it is not clear which factor plays the predominant role. Precipitation from each reanalysis also shows differences (Figure S2 in Supporting Information S1). ERA5 has the highest temporal, spatial, and vertical resolution and all the reanalyzes have unique convective schemes. ERA5 and JRA-55 use a four dimensional variational (4D-Var) data assimilation scheme, while MERRA-2 and NCEP-NCAR use a three dimensional variational (3D-Var) scheme. Both ERA5 and JRA-55 assimilated the OTREC dropsondes and employ 4D-Var so we believe that the disagreement between ERA5 and JRA-55 is probably more related to the convective scheme and spatial resolution.

HUAMAN ET AL. 4 of 10



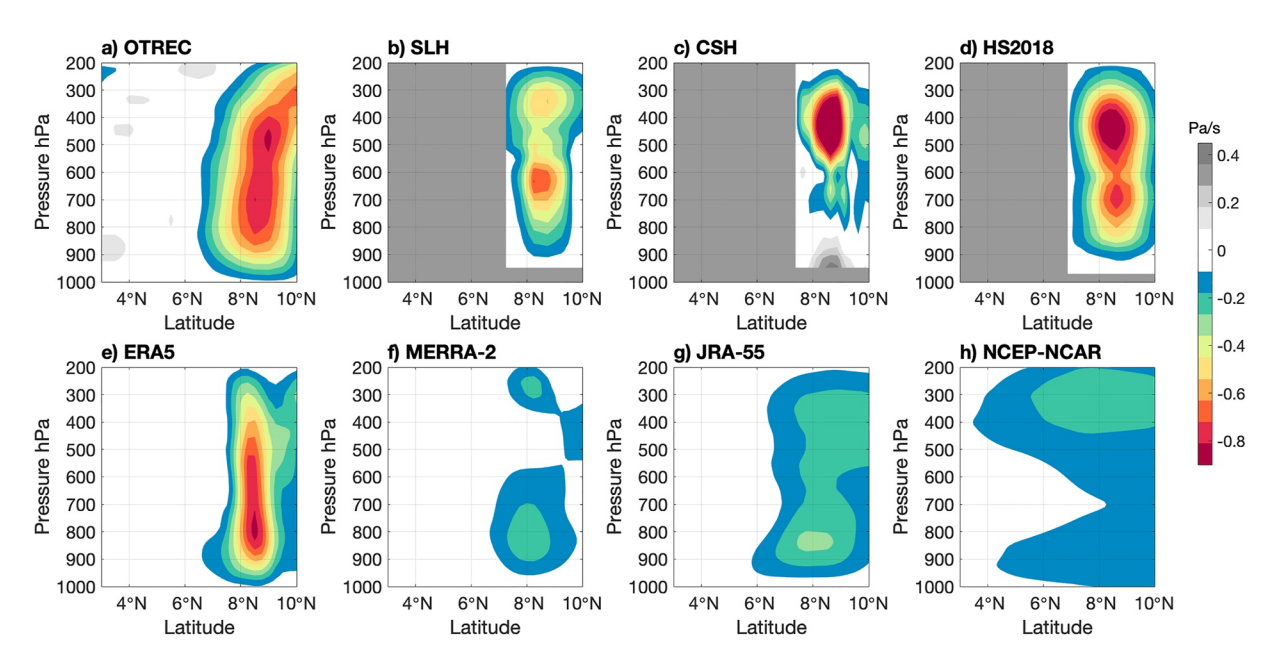


Figure 2. Vertical cross sections of vertical motion in Pa s⁻¹ across 89°–86°W during RF14 (21 September 2019), from (a) OTREC dropsondes averaged for 12–18 UTC, (b–d) GPM algorithms (SLH, CSH, and HS2018) at 16 UTC, and (e–h) reanalyzes (ERA5, MERRA2, JRA55, and NCEP-NCAR) averaged for 12–18 UTC.

Only RF 14 (21 September, 2019) coincided with a GPM overpass in the OTREC flight box and 12–18 UTC time window. A strong convective system was centered in the northeast part of the OTREC box and was well captured by a GPM swath at 16 UTC. The precipitation associated with the convective system had similar precipitation intensity and position at 16 UTC (GPM snapshot time) compared to the 12–18 UTC average (not shown). Vertical velocity profiles from OTREC dropsondes for 12–18 UTC, GPM algorithms for 16 UTC and reanalyzes for 12–18 UTC on 21 September are shown in Figure 2 and indicate active deep ascending motion in the northern portion of the OTREC box. OTREC observations (Figure 2a) show strong upward motion, up to $-0.9 \, \mathrm{Pa} \, \mathrm{s}^{-1}$, throughout the troposphere. GPM products also show strong deep vertical motion. SLH (Figure 2b) has upward motion throughout the troposphere, although less intense than the OTREC dropsondes, with a vertical velocity peak around 650 hPa. CSH (Figure 2c) shows strong upward motion around 400 hPa and weaker downward motion from 700 hPa to the surface due to evaporative cooling below cloud base in the stratiform rain region. HS2018 (Figure 2d) has strong upward motion through the depth of the troposphere, similar to OTREC observations.

Reanalyzes indicate different vertical motion structures on this day, except ERA5. ERA5 vertical velocity (Figure 2e) shows strong upward motion with values up to -0.9 Pa s^{-1} from 850 to 500 hPa, similar to OTREC but shifted slightly lower in the troposphere. MERRA-2, JRA-55, and NCEP-NCAR (Figures 2f-2h) show weak vertical velocities with values between -0.1 and -0.3 Pa s^{-1} and a predominant shallow mode peaking at 850 hPa throughout the EP ITCZ. The disagreement between reanalyzes is partially explained by the resolution dependency in each reanalysis. However, JRA-55 provides a more realistic vertical motion profile than MERRA-2 despite its coarser resolution, suggesting that some benefit is still being provided through assimilation of the OTREC dropsonde data.

4. Monte Carlo Analysis

Although we presented a comprehensive case study from the OTREC field campaign in Section 3, the comparison to GPM data was limited by the near absence of coincident overpasses. In an attempt to make a more representative comparison, we looked for all the GPM radar overpasses in the OTREC flight box with precipitation data available between 4°N-9°N and from 12 to 18 UTC for August and September during 2014–2020, and found 42 samples. The vertical velocity average derived from the GPM latent heating algorithms for the 42 overpasses is shown in Figures 3b–3d. Vertical velocity averages for 12–18 UTC from MERRA-2, JRA-55, and NCEP-NCAR for the same 42 GPM dates are shown in Figures 3e–3h. For easier comparison with the OTREC observations, we repeat the OTREC vertical motion average from Figure 1b as panel Figure 3a.

HUAMAN ET AL. 5 of 10

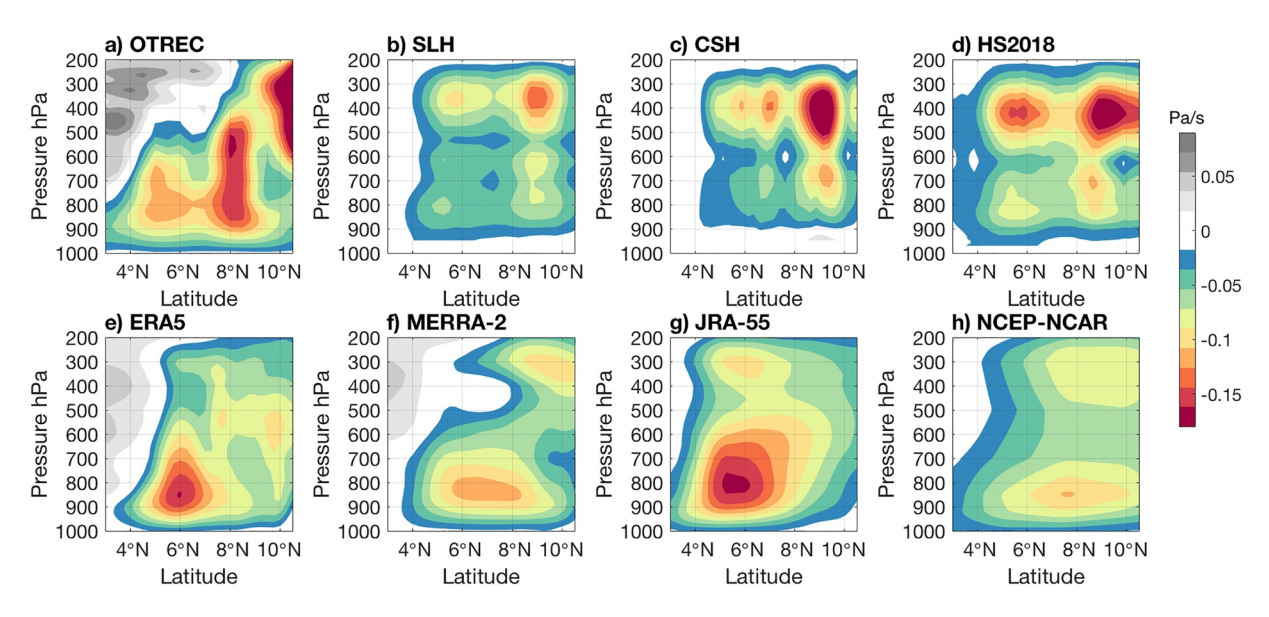


Figure 3. Vertical cross sections of vertical motion in Pa s⁻¹ across 89°–86°W from (a) OTREC dropsondes averaged over the nine RF samples, (b–d) GPM algorithms and (e–h) reanalyzes averaged over the GPM 42 days sample dates between August and September and 2014–2020 and 12–18 UTC.

Figure 3 shows that all of the GPM algorithms produce deep upward motion at 6°N and 9°N. Shallow upward motion predominates in the reanalyzes around 6°N and is stronger in JRA-55 and ERA5 than MERRA-2 and NCEP-NCAR. We note that the vertical velocity climatologies for 2014–2020 are similar to the 42-day averages in all of the reanalyzes (not shown). Figure 3 calls attention to the significant disagreement between GPM algorithms and reanalyzes. While reanalyzes generally suggest stronger shallow vertical motion over much of the EP ITCZ, GPM algorithms indicate a predominance of deep vertical motion.

To conduct a more robust assessment of the vertical velocity in the EP ITCZ, we performed a Monte Carlo analysis in which we constructed numerous random 9-day sample averages among the 42-day samples from GPM and reanalyzes that were expected to be comparable with the OTREC field campaign data. The results of this analysis for three latitude bands (i.e., 4°–7.5°N, 7.5°–9°N, and 9°–10.5°N) are shown in Figure 4. We performed a 9-day average 1,000 times and display the results as a set of colored points every 100 hPa representing the minimum average, 25th percentile, mean, 75th percentile, and maximum average vertical motion value for each GPM algorithm and reanalysis. We interpret as a good approximation of vertical velocity from the GPM algorithms or reanalysis data when their mean is inside the OTREC standard error range (i.e., gray profiles in Figure 4) and their interquartile range (i.e., the range between the 25th and 75th percentiles) includes the OTREC mean.

In the southern part of the EP ITCZ (4° –7.5°N; Figure 4a), the OTREC dropsondes indicate a well-defined shallow vertical motion peak with a vertical velocities up to -0.1 Pa s⁻¹ at 850 hPa. The Monte Carlo distributions of the GPM satellite products show a vertical velocity around -0.05 Pa s⁻¹ at 850 hPa and closer to -0.1 Pa s⁻¹ above 500 hPa; however, the dispersion distribution is wide at higher levels. Thus, the GPM vertical motion is too weak at low levels and too strong aloft compared to the OTREC observations. At low levels, the underestimation is likely associated with the sensitivity of the radar installed on GPM. To test this theory, we replaced the GPM shallow precipitation with the climatological CloudSat shallow precipitation from Huaman and Schumacher (2018) for August and September making the total precipitation the sum of the GPM stratiform, GPM convective, and CloudSat shallow precipitation. The extra shallow precipitation measured by CloudSat increases latent heating at low levels and therefore vertical velocity (open circles in Figure 4a) and is more consistent with OTREC observations. At higher levels, the OTREC observations indicate descending motion on the order of 0.05 Pa s⁻¹ and dry conditions (Figure S3a in Supporting Information S1). We disregard radiative cooling in our simplified thermodynamic equation and the large-scale circulation (i.e., descending motion from the Walker and Hadley cells), which contributes to the overestimation of vertical velocity from GPM algorithms at upper levels, especially in the southern region.

HUAMAN ET AL. 6 of 10

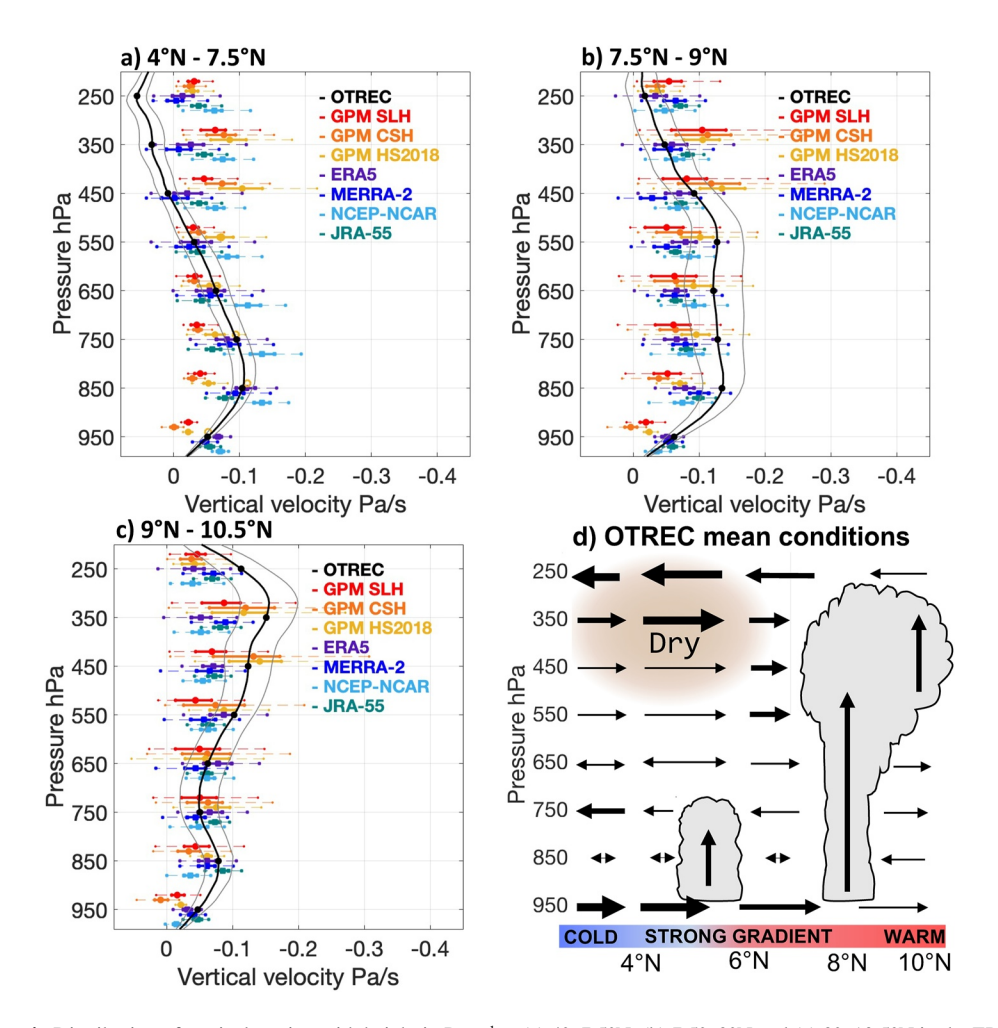


Figure 4. Distribution of vertical motion with height in Pa s⁻¹ at (a) 4° –7.5°N, (b) 7.5° –9°N and (c) 9° –10.5°N in the EP ITCZ based on Monte Carlo analysis using 42 samples between 2014 and 2020 from the GPM algorithms and reanalyzes. Each set of points represent the minimum average, 25th percentile, mean, 75th percentile, and maximum average. The black profile shows the OTREC vertical velocity 9-day sample mean (averaged over the 9 RFs) with standard error in gray lines. The yellow open circles in panel (a) indicates GPM/CloudSat HS2018 vertical velocity. (d) Sketch of the OTREC mean conditions of the meridional overturning circulation over the East Pacific ITCZ. The thin, thick, and thickest horizontal vectors indicate meridional winds smaller than 2 m s⁻¹, between 2 and 4 m s⁻¹, and larger than 4 m s⁻¹, respectively. The short double arrow indicates meridional winds around 0 m s⁻¹.

All of the reanalysis Monte Carlo distributions show a shallow peak of vertical velocity at 850 hPa from 4° to 7.5°N (Figure 4a) that is consistent with the OTREC observations and only JRA-55 and NCEP-NCAR mean values are outside of the OTREC dispersion range. Above 550 hPa, vertical velocities from reanalyzes are larger than the OTREC observations and may be related to the small static stability of the atmosphere (i.e., $d\theta/dz$) over this region. The vertical motion can be approximately determined by dividing the diabatic heating rate $(d\theta/dt)$ by the static stability of the atmosphere (Mapes & Houze Jr, 1995; Raymond & Zeng, 2005; Sobel et al., 2001). When the static stability is very small, as it tends to be in the tropical upper troposphere (because the moist adiabats become close to dry adiabats at low temperature), vertical motion is large even if the diabatic heating is small, and any signals (or errors) in the heating will be amplified by the small denominator.

In the northern part of the ITCZ, OTREC dropsondes show two deep vertical motion peaks at 7.5°–9°N and 9°–10.5°N (Figure 3a), which are retrieved by the GPM satellite products as single deep peak between 7.5° and 10.5°N (Figures 3b–3d). Between 7.5°N and 9°N (Figure 4b), OTREC upward motion is around 0.12 Pa s⁻¹ between 850 hPa and 550 hPa and the vertical motion from the reanalyzes and GPM Monte Carlo simulations are generally too weak. The GPM underestimation is not fully explained by the shallow precipitation from CloudSat, which is similar to the GPM precipitation over these latitudes. It is unclear why the reanalyzes become too weak

HUAMAN ET AL. 7 of 10



at low levels in this region. Above 450 hPa, GPM satellite products remain overly strong, whereas the reanalyzes become more consistent with OTREC observations.

Between 9° and 10.5°N (Figure 4c), the OTREC observations show deep upward motion with a maximum at 350 hPa, a profile that is normally associated with organized convective systems. However, a small secondary peak at 850 hPa suggests the presence of at least some shallow convection. The GPM Monte Carlo distributions for CSH and HS2018 are generally consistent with the OTREC dropsondes throughout the profile, whereas SLH becomes too weak aloft. Reanalyzes are back to being consistent with the OTREC observations below 550 hPa, but become weaker above. The average of the two OTREC deep vertical motion peaks between 7.5° and 10.5°N is shown in Figure S4 in Supporting Information S1. Overall, the deep mode structure shown by the OTREC observations is supported by the GPM algorithms, but not by reanalyzes.

Figure 4d presents a diagram of the overturning meridional circulation of the EP ITCZ based on OTREC observations. Supporting cross sections of the meridional winds and mixing ratio from OTREC dropsondes are shown in Figure S3 in Supporting Information S1. Winds were southerly at the surface, consistent with Raymond et al. (2004), and extended up to 850 hPa. The southerly surface trade winds converged around 5°N, where the meridional SST gradient is strong, and northerly return flow was present around 750 hPa. A southerly midlevel inflow was seen between 550 and 350 hPa, consistent with Huaman and Takahashi (2016). Above the shallow circulation, a dry layer associated with the descending motion of the Walker circulation (Wang & Enfield, 2003) was predominant. A deep circulation was seen to the north with deep vertical motion at 8°N and 10°N where SST is warmest, with a strong overturning and diverging circulation around 250 hPa.

5. Summary and Conclusions

We assessed the vertical velocity structure in the EP ITCZ using dropsondes from the OTREC 2019 field campaign, latent heating retrievals from the GPM satellite radar, and vertical velocity fields from reanalyzes. OTREC observations indicated a shallow mode from 3° to 7°N, over a strong meridional gradient in SST, but a deep mode farther north, where the SST is warmest. However, all the reanalyzes (albeit with different intensities) showed a predominant shallow mode from 3° to 10°N across the EP ITCZ unless they assimilated the dropsondes, as was done by ERA5 and JRA-55. Then a weak deep mode was produced further north. Only ERA5 and MERRA-2 retrieved the vertical velocity correctly around 4°-7.5°N according to our criteria described in Section 4. The reanalyzes represent a range of resolutions, convective parameterizations, and assimilation schemes so it is unclear why they all have difficulty deepening convection over the EP ITCZ. Vertical motion derived from the GPM latent heating algorithms, especially GPM CSH and HS2018, indicated deep vertical motions from 3° to 10°N, consistent with the OTREC observations. The lack of a shallow mode is due to the inability of the GPM radar to sense weakly precipitating shallow convection, but the addition of cloud radar data can ameliorate the issue. The OTREC 2019 field campaign observations were crucial to identify deficiencies in the reanalyzes and GPM algorithms. Reanalyzes, especially MERRA2 and NCEP-NCAR, underestimate the deep vertical motion seen in the northern part of the EP ITCZ and GPM algorithms, especially SLH, underestimate the shallow vertical motion in southern part of the EP ITCZ. The inability of reanalyzes to retrieve the correct vertical velocity structure is likely related to the physical parameterizations and spatial resolution of the parent models, while the satellite retrievals suffer from the underestimation of light precipitation associated with the sensitivity of the radars onboard the TRMM and GPM satellites.

Data Availability Statement

The data used in this study were acquired from Zenodo science (3DVar OTREC data; https://zenodo.org/record/5152171#.YaQEXS-cZ-U), Goddard Earth System division and Information Service Center (GPM CSH and SLH and MERRA-2; http://disc.sci.gsfc.nasa.gov/), ECMWF (ERA5; https://www.ecmwf.int/en/forecasts/datasets/reanalysis-datasets/era5/), NOAA/ESRL (NCEP-NCAR; http://www.esrl.noaa.gov/psd/), and NCAR/UCAR research data archive (JRA, https://rda.ucar.edu).

HUAMAN ET AL. 8 of 10



Acknowledgments

This work was supported by a NASA Earth and Space Science Fellowship (NESSF) under grant 80NSSC18K1402. The authors also thank Larissa Back for useful discussions and comments.

References

- Arakawa, A., & Schubert, W. H. (1974). Interaction of a cumulus cloud ensemble with the large-scale environment, Part I. *Journal of the Atmospheric Sciences*, 31(3), 674–701. https://doi.org/10.1175/1520-0469(1974)031<0674:ioacce>2.0.co;2
- Back, L., & Bretherton, C. (2006). Geographic variability in the export of moist static energy and vertical motion profiles in the tropical Pacific. Geophysical Research Letters, 33(17). https://doi.org/10.1029/2006gl026672
- Donlon, C. J., Martin, M., Stark, J., Roberts-Jones, J., Fiedler, E., & Wimmer, W. (2012). The operational sea surface temperature and sea ice analysis (ostia) system. Remote Sensing of Environment, 116, 140–158. https://doi.org/10.1016/j.rse.2010.10.017
- Frierson, D. M. W. (2007). The dynamics of idealized convection schemes and their effect on the zonally averaged tropical circulation. *Journal of the Atmospheric Sciences*, 64, 1959–1976. https://doi.org/10.1175/jas3935.1
- Fuchs-Stone, Ž., Raymond, D. J., & Sentić, S. (2020). OTREC2019: Convection over the east Pacific and southwest Caribbean. *Geophysical Research Letters*, 47(11), e2020GL087564. https://doi.org/10.1029/2020GL087564
- Gelaro, R., McCarty, W., Suárez, M. J., Todling, R., Molod, A., Takacs, L., et al. (2017). The modern-era retrospective analysis for research and applications, version 2 (MERRA-2). *Journal of Climate*, 30(14), 5419–5454. https://doi.org/10.1175/jcli-d-16-0758.1
- Hagos, S., Zhang, C., Tao, W. -K., Lang, S., Takayabu, Y. N., Shige, S., et al. (2010). Estimates of tropical diabatic heating profiles: Commonalities and uncertainties. *Journal of Climate*, 23(3), 542–558. https://doi.org/10.1175/2009jcli3025.1
- Hersbach, H., Bell, B., Berrisford, P., Hirahara, S., Horányi, A., Muñoz-Sabater, J., et al. (2020). The ERA5 global reanalysis. *Quarterly Journal of the Royal Meteorological Society*, 146(730), 1999–2049. https://doi.org/10.1002/qj.3803
- Hou, A. Y., Kakar, R. K., Neeck, S., Azarbarzin, A. A., Kummerow, C. D., Kojima, M., et al. (2014). The global precipitation measurement mission. Bulletin of the American Meteorological Society, 95(5), 701–722. https://doi.org/10.1175/bams-d-13-00164.1
- Houze, R. A. (1989). Observed structure of mesoscale convective systems and implications for large-scale heating. Quarterly Journal of the Royal Meteorological Society, 115(487), 425–461. https://doi.org/10.1002/qj.49711548702
- Huaman, L., Maloney, E. D., Schumacher, C., & Kiladis, G. N. (2021). Easterly waves in the East Pacific during the otrec 2019 field campaign. Journal of the Atmospheric Sciences. 78. https://doi.org/10.1175/JAS-D-21-0128.1
- Huaman, L., & Schumacher, C. (2018). Assessing the vertical latent heating structure of the East Pacific ITCZ using the CloudSat CPR and TRMM PR. *Journal of Climate*, 31(7), 2563–2577. https://doi.org/10.1175/jcli-d-17-0590.1
- Huaman, L., Schumacher, C., & Kiladis, G. N. (2020). Eastward-propagating disturbances in the tropical pacific. *Monthly Weather Review*, 148(9), 3713–3728. https://doi.org/10.1175/mwr-d-20-0029.1
- Huaman, L., & Takahashi, K. (2016). The vertical structure of the eastern Pacific ITCZs and associated circulation using the TRMM Precipitation Radar and in situ data. *Geophysical Research Letters*, 43(15), 8230–8239. https://doi.org/10.1002/2016g1068835
- Huffman, G. J., Bolvin, D. T., Braithwaite, D., Hsu, K., Joyce, R., Xie, P., & Yoo, S. -H. (2015). NASA global precipitation measurement (GPM) integrated multi-satellite retrievals for GPM (IMERG). Algorithm Theoretical Basis Document (ATBD) Version, 4, 26.
- Inoue, K., & Back, L. E. (2015). Gross moist stability assessment during toga coare: Various interpretations of gross moist stability. *Journal of the Atmospheric Sciences*, 72(11), 4148–4166. https://doi.org/10.1175/jas-d-15-0092.1
- Kiladis, G. N., Dias, J., Straub, K. H., Wheeler, M. C., Tulich, S. N., Kikuchi, K., et al. (2014). A comparison of OLR and circulation-based indices for tracking the MJO. *Monthly Weather Review*, 142(5), 1697–1715.
- Kobayashi, S., Ota, Y., Harada, Y., Ebita, A., Moriya, M., Onoda, H., et al. (2015). The JRA-55 reanalysis: General specifications and basic characteristics. *Journal of the Meteorological Society of Japan. Series II*, 93(1), 5–48. https://doi.org/10.2151/jmsj.2015-001
- Liu, C., Shige, S., Takayabu, Y. N., & Zipser, E. (2015). Latent heating contribution from precipitation systems with different sizes, depths, and intensities in the tropics. *Journal of Climate*, 28(1), 186–203. https://doi.org/10.1175/jcli-d-14-00370.1
- Mapes, B. E., & Houze, R. A., Jr. (1995). Diabatic divergence profiles in western pacific mesoscale convective systems. *Journal of the Atmospheric Sciences*, 52(10), 1807–1828. https://doi.org/10.1175/1520-0469(1995)052<1807:ddpiwp>2.0.co;2
- Moorthi, S., & Suarez, M. J. (1992). Relaxed Arakawa-Schubert: A parameterization of moist convection for general circulation models. *Monthly Weather Review*, 120(6), 978–1002. https://doi.org/10.1175/1520-0493(1992)120<0978:rasapo>2.0.co;2
- Neelin, J. D., & Held, I. M. (1987). Modeling tropical convergence based on the moist static energy budget. *Monthly Weather Review*, 115, 3–12. https://doi.org/10.1175/1520-0493(1987)115<0003:mtcbot>2.0.co;2
- Nolan, D. S., Zhang, C., & Chen, S.-h. (2007). Dynamics of the shallow meridional circulation around intertropical convergence zones. *Journal of the Atmospheric Sciences*, 64(7), 2262–2285. https://doi.org/10.1175/jas3964.1
- Numaguti, A. (1993). Dynamics and energy balance of the Hadley circulation and the tropical precipitation zones: Significance of the distribution of evaporation. *Journal of the Atmospheric Sciences*, 50(13), 1874–1887. https://doi.org/10.1175/1520-0469(1993)050<1874:daebot>2.0.co;2
- Pan, H. -l., & Wu, W. -S. (1995). Implementing a mass flux convection parameterization package for the NMC medium-range forecast model.
- Raymond, D. J., Esbensen, S. K., Paulson, C., Gregg, M., Bretherton, C. S., Petersen, W. A., et al. (2004). EPIC2001 and the coupled ocean-atmosphere system of the tropical east Pacific. Bulletin of the American Meteorological Society, 85(9), 1341–1354. https://doi.org/10.1175/bams-85-9-1341
- Raymond, D. J., Sessions, S., Sobel, A. H., & Fuchs, Z. (2009). The mechanics of gross moist stability. *Journal of Advances in Modeling Earth Systems*, 1. https://doi.org/10.3894/JAMES.2009.1.9
- Raymond, D. J., & Zeng, X. (2005). Modelling tropical atmospheric convection in the context of the weak temperature gradient approximation. Quarterly Journal of the Royal Meteorological Society, 131(608), 1301–1320. https://doi.org/10.1256/qj.03.97
- Saha, S., Moorthi, S., Wu, X., Wang, J., Nadiga, S., Tripp, P., et al. (2014). The NCEP climate forecast system version 2. *Journal of Climate*, 27(6), 2185–2208. https://doi.org/10.1175/jcli-d-12-00823.1
- Schumacher, C., Houze, R. A., Jr, & Kraucunas, I. (2004). The tropical dynamical response to latent heating estimates derived from the TRMM precipitation radar. *Journal of the Atmospheric Sciences*, 61(12), 1341–1358. https://doi.org/10.1175/1520-0469(2004)061<1341:ttdrtl>2.0.co;2
- Shige, S., Takayabu, Y. N., Kida, S., Tao, W.-K., Zeng, X., Yokoyama, C., & L'Ecuyer, T. (2009). Spectral retrieval of latent heating profiles from TRMM PR data. Part IV: Comparisons of lookup tables from two-and three-dimensional cloud-resolving model simulations. *Journal of Climate*, 22(20), 5577–5594. https://doi.org/10.1175/2009jcli2919.1
- Shige, S., Takayabu, Y. N., Tao, W.-K., & Johnson, D. E. (2004). Spectral retrieval of latent heating profiles from TRMM PR data. Part I: Development of a model-based algorithm. *Journal of Applied Meteorology*, 43(8), 1095–1113. https://doi.org/10.1175/1520-0450(2004)043<1095:s-rolhp>2.0.co;2
- Shige, S., Takayabu, Y. N., Tao, W. -K., & Shie, C. -L. (2007). Spectral retrieval of latent heating profiles from TRMM PR data. Part II: Algorithm improvement and heating estimates over tropical ocean regions. *Journal of Applied Meteorology and Climatology*, 46(7), 1098–1124. https://doi.org/10.1175/jam2510.1

HUAMAN ET AL. 9 of 10



- Sobel, A. H. (2007). Simple models of ensemble-averaged tropical precipitation and surface wind. In Schneider, T., & Sobel, A. H. (Eds.), *The global circulation of the atmosphere* (pp. 219–251). Princeton University Press.
- Sobel, A. H., Nilsson, J., & Polvani, L. M. (2001). The weak temperature gradient approximation and balanced tropical moisture waves. *Journal of the Atmospheric Sciences*, 58(23), 3650–3665. https://doi.org/10.1175/1520-0469(2001)058<3650:twtgaa>2.0.co;2
- Tao, W.-K., Lang, S., Olson, W., Meneghini, R., Yang, S., Simpson, J., et al. (2001). Retrieved vertical profiles of latent heat release using TRMM rainfall products for February 1998. *Journal of Applied Meteorology*, 40(6), 957–982. https://doi.org/10.1175/1520-0450(2001)040<0957:r vpolh>2.0.co;2
- Tao, W.-K., Lang, S., Zeng, X., Shige, S., & Takayabu, Y. (2010). Relating convective and stratiform rain to latent heating. *Journal of Climate*, 23(7), 1874–1893. https://doi.org/10.1175/2009jcli3278.1
- Tiedtke, M. (1989). A comprehensive mass flux scheme for cumulus parameterization in large-scale models. *Monthly Weather Review*, 117(8), 1779–1800. https://doi.org/10.1175/1520-0493(1989)117<1779;acmfsf>2.0.co;2
- Trenberth, K. E., Stepaniak, D. P., & Caron, J. M. (2000). The global monsoon as seen through the divergent atmospheric circulation. *Journal of Climate*, 13(22), 3969–3993. https://doi.org/10.1175/1520-0442(2000)013<3969:tgmast>2.0.co;2
- Wang, C., & Enfield, D. B. (2003). A further study of the tropical Western Hemisphere warm pool. *Journal of Climate*, 16(10), 1476–1493. https://doi.org/10.1175/1520-0442-16.10.1476
- Yokoyama, C., Zipser, E. J., & Liu, C. (2014). TRMM-observed shallow versus deep convection in the eastern pacific related to large-scale circulations in reanalysis datasets. *Journal of Climate*, 27(14), 5575–5592. https://doi.org/10.1175/jcli-d-13-00315.1
- Yu, J. Y., Chou, C., & Neelin, J. D. (1998). Estimating the gross moist stability of the tropical atmosphere. *Journal of the Atmospheric Sciences*, 55, 1354–1372. https://doi.org/10.1175/1520-0469(1998)055<1354:etgmso>2.0.co;2
- Zhang, C., McGauley, M., & Bond, N. A. (2004). Shallow meridional circulation in the tropical eastern Pacific. *Journal of Climate*, 17(1), 133–139. https://doi.org/10.1175/1520-0442(2004)017<0133:smcitt>2.0.co;2
- Zhang, C., Nolan, D. S., Thorncroft, C. D., & Nguyen, H. (2008). Shallow meridional circulations in the tropical atmosphere. *Journal of Climate*, 21(14), 3453–3470. https://doi.org/10.1175/2007jcli1870.1

HUAMAN ET AL. 10 of 10